

Direct observation of indium precipitates in silicon following high dose ion implantation

K J Dudeck¹, E Huante-Ceron², A P Knights², R M Gwilliam³
and G A Botton¹

¹ Department of Materials Science and Engineering, McMaster University, 1280 Main Street West, Hamilton, ON L8S 4L7, Canada

² Department of Engineering Physics, McMaster University, 1280 Main Street West, Hamilton, ON L8S 4L7, Canada

³ Surrey Ion Beam Centre, University of Surrey, Guildford, Surrey, GU2 7XH, UK

E-mail: dudeckkj@mcmaster.ca and gbotton@mcmaster.ca

Received 15 July 2013, in final form 20 September 2013

Published 7 November 2013

Online at stacks.iop.org/SST/28/125012

Abstract

We present electron microscopy, electrical measurement and secondary ion mass spectroscopy (SIMS) characterization of silicon doped with indium to concentrations well above the assumed solid solubility. Samples have been prepared using ion implantation at an energy of 40 keV to achieve as-implanted indium concentrations up to $1 \times 10^{20} \text{ cm}^{-3}$, with post-implantation annealing performed at temperatures between 600 and 1050 °C. We provide direct evidence for nano-scale indium precipitates in the silicon matrix and on the sample surface after annealing. Precipitates having a tetragonal crystal structure and a rectangular shape were observed in all of the samples implanted at the highest dose of $1 \times 10^{15} \text{ cm}^{-2}$, and some of the samples implanted with a lower dose. Comparing SIMS and electron microscopy data allows us to conclude a solid solubility of $\approx 10^{18} \text{ cm}^{-3}$, consistent with previously published work (Solmi *et al* 2002 *J. Appl. Phys.* **92** 1361–6). This paper determines the limitations of indium utility as a dopant in silicon with regard to solid solubility and dose loss. The latter is in excess of 75% for samples annealed at temperatures at and above 750 °C.

1. Introduction

Indium remains an important alternative to boron as a p-type dopant of silicon. Its relatively high mass should allow, in principle, the formation of shallow junctions via ion implantation, whose concentration distribution is extremely narrow. Further, the ability to engineer steep retrograde p-type profiles using indium has been enabling in the engineering of *n*-channel silicon devices [2, 3].

A number of studies have attempted to quantify the properties of ion implanted and subsequently annealed indium doped silicon, and the associated free holes. In general, it has been shown that electrical and chemical characteristics are consistent with a solid solubility of a few 10^{18} cm^{-3} [1]. Given that the indium associated acceptor level is 157 meV above the valence band edge, this solid solubility value limits the free hole carrier concentration at

room temperature to approximately $2\text{--}3 \times 10^{17} \text{ cm}^{-3}$. This prevents the use of indium as a dopant for source and drain contact applications where carrier concentrations in excess of 10^{20} cm^{-3} are required, but permits the use of indium for channel engineering. There is some evidence that co-doping indium with carbon increases the active concentration through the formation of a carbon–indium complex, which is positioned closer to the valence band edge, however this co-doping approach has not led to widespread application [4–6].

Despite the previous attempts at quantification of the limitations of indium as a silicon dopant (mostly via electrical and secondary ion mass spectroscopy (SIMS) analysis [1, 7, 8]), there remains no information on the nature of excess indium in silicon on the atomic scale. For instance, it is not clear that indium readily clusters to form nano-scale inclusions. Indeed the lack of direct observation of indium

nano-clusters limits the strength of any assertion that one may make regarding the absolute value of solid solubility and thus the fraction of electrically active dopant. There also remains little or no information on the processes which govern the significant dose loss of indium during activation annealing, a phenomenon which plays an important role in reducing the utility of the dopant [1].

In this paper we describe fabrication of samples via ion implantation and annealing of silicon using indium doses greatly in excess of those required to produce doped regions at concentrations significantly above the assumed solid solubility limit. Specifically, the indium ions were implanted at 40 keV at doses ranging from 1×10^{14} to $1 \times 10^{15} \text{ cm}^{-2}$, producing as-implanted peak concentrations ranging from 1×10^{19} to $1 \times 10^{20} \text{ cm}^{-3}$. We have combined electron microscopy, SIMS and electrical (Hall) measurements to assess solid solubility which we confirm to be in agreement with previous work at $\approx 2 \times 10^{18} \text{ cm}^{-3}$. We use high angle annular dark field scanning transmission electron microscopy (HAADF STEM) and electron energy loss (EEL) spectroscopy and spectrum imaging (SI) elemental mapping to determine how the indium atoms are redistributed after annealing. Clusters of pure indium are conclusively observed for the first time both on the surface and in the sub-surface region and their size and location are determined. We compare the HAADF STEM results with conventional transmission electron microscopy (CTEM) analysis, which is prevalent in the research literature, in order to assess the potential for the two techniques in characterizing heavy dopant distributions in silicon. We have compared the electron microscopy results with Hall and SIMS measurements to gauge the activation and distribution of dopant atoms that are not clustered and find that indium redistributes rapidly, likely due to transient enhanced diffusion driven by the excess silicon interstitials present after implantation. We note that most of the indium implanted at these high doses is lost from the surface of the silicon during the post-implantation annealing step.

2. Experimental details

2.1. Material preparation

Samples consisting of electrical junctions (thus suitable for electrical measurement) were prepared by implanting indium ions into n-type, phosphorus-doped (100) silicon (initial concentration of $\approx 1 \times 10^{15} \text{ cm}^{-3}$) at four doses (dose A: 1×10^{15} ; dose B: 7×10^{14} ; dose C: 3×10^{14} ; and dose D: $1 \times 10^{14} \text{ cm}^{-2}$), followed by thermal annealing. All implants used an energy of 40 keV and an angle of 7° to the surface normal to prevent excessive channeling. The total beam current density was approximately $0.3 \mu\text{A cm}^{-2}$. Considering the implantation energy of 40 keV and the fact that the wafer was in good thermal contact to a heat sink, no significant temperature rise of the substrate was anticipated during implantation, and certainly it was less than 50°C following previous calibration of the implantation system. Such implantation conditions produce an amorphous layer of $\approx 50 \text{ nm}$ thickness from the surface. The wafers had a screen oxide with a thickness no greater than 10 nm. Following implantation, samples were

annealed at four temperatures (600, 750, 950 and 1050°C) for 2 min in a N_2 atmosphere using a rapid thermal annealing apparatus. Henceforth the samples will be referred to by a letter representing the implant dose (i.e., dose A, B, C or D, as noted above) and a number representing the annealing temperature in degrees Celsius (600, 750, 950 or 1050), i.e. sample A750 indicates the samples implanted with a dose of $1 \times 10^{15} \text{ cm}^{-2}$ and annealed at a temperature of 750°C .

2.2. Electron microscopy

Material implanted at doses A and C (as-implanted and annealed at all four temperatures) were analyzed using CTEM, HAADF STEM and EEL SI. While CTEM has been extensively used to study defects following ion implantation (e.g. see [7–10]), the contrast mechanism is not specifically sensitive to heavy dopants in a light-atom matrix (such as indium in silicon).

HAADF STEM images are formed by scanning a small probe over the surface of the sample and collecting transmitted electrons scattered to high angles. HAADF STEM is an ideal technique for probing distributions of heavy dopants in silicon because it is an incoherent imaging mode where the image intensity is proportional to approximately the square of the atomic number, Z (i.e. $I \approx Z^2$) [11, 12]. Hence, HAADF STEM is often referred to as Z -contrast imaging. In the case of indium implanted in silicon, we expect the intensity of dopant indium to be ≈ 12 times higher than that of host silicon ($Z_{\text{In}} = 49$, $Z_{\text{Si}} = 14$). Due to the utility of HAADF STEM in discerning indium from silicon, this was the primary electron microscopy analysis method used for this work although CTEM and HAADF STEM images will be compared briefly in section 3.

When scattering through the TEM specimen, some of the incident electrons undergo inelastic scattering and lose energy, for example, due to ionization of inner-shell electrons. EEL spectroscopy measures the energy lost by these electrons using an electron spectrometer below the specimen. Individual EEL spectra are acquired as the beam is rastered over a two-dimensional area to produce a map of the energy loss as a function of position; this technique is referred to as STEM EEL SI and can be performed simultaneously with collection of HAADF STEM data. EEL spectroscopy and SI allow us to probe the chemical nature of the dopants in order to determine the constituent atomic species [13].

Electron microscopy specimens were prepared in a cross-sectional configuration by tripod polishing combined with low voltage ($< 800 \text{ V}$) ion milling. Tripod polishing was performed using an Allied Multiprep semi-automated polisher with initial sample material consisting of two pieces of sample material (each approximately 1 mm^2) glued together in a cross-sectional configuration. The top and bottom sides of the sample were polished planar to a thickness of approximately $100 \mu\text{m}$ before a 2° wedge was introduced. Diamond lapping films having particle size 0.1 to $30 \mu\text{m}$ were used on both sides of the specimen. Following polishing, the wedge was attached to a slot grid and ion milling was performed using a Technoorg Linda Gentle Mill operating with an argon ion beam having energies between 350 and 800 eV at angles ranging between 6° and 11° relative to the specimen plane.

All samples were initially imaged using diffraction contrast in a Philips CM12 CTEM operating at 120 kV in order to assess defect and dopant distributions before and after ion milling, to ensure that the ion milling did not introduce any artifacts. HAADF STEM and EEL SI were performed using a FEI-Titan 80–300 STEM operated at 200 kV and equipped with two aberration correctors. The samples were imaged with the silicon matrix in the $[0\bar{1}\bar{1}]$ direction and oriented such that the surface was parallel to the top of the image. Some images were collected with the silicon matrix tilted $\approx 4^\circ$ away from the $[0\bar{1}\bar{1}]$ zone axis in order to reduce the electron channeling effect caused by the atomic columns and thus increase the visibility of the dopant atoms. Unless otherwise noted, all images shown in this paper will be oriented with the surface towards the top of the image and with the silicon matrix on the $[0\bar{1}\bar{1}]$ zone axis.

For HAADF STEM imaging, a convergence angle of 19 mrad and detector inner semiangle of 75 mrad were employed. STEM EEL SI data was collected with dwell times of 30–40 ms, 0.5 eV/channel, a convergence angle of 19 mrad and collection angle of 80 mrad; drift correction was not employed during data acquisition. EEL spectroscopy was used to determine a specimen thickness of $(15\text{--}50) \pm 5$ nm in the areas analyzed using the mean-free path of total inelastic scattering [13].

2.3. Hall measurements

Hall measurements using the van der Pauw configuration were performed using an Accent HL5500PC Hall effect system. Attempts at measurement were made for all annealed samples for all implant doses and all annealing temperatures. Prior to performing the measurements, the samples were cleaned using a three step process: (1) H_2SO_4 for <5 min to remove surface organics; (2) HCl solution (100 ml de-ionized water, 25 ml H_2O_2 and 25 ml HCl) for 5 min to remove any metallic contamination (predominantly that caused by indium precipitates on the surface); (3) HF dip for 1 min to remove the surface oxide, followed by two water baths and a 5 min rinse in fresh de-ionized water. Electrical contact to the sample surface was made using the electro-forming technique with ohmicity being confirmed prior to each measurement through observation of the sample I – V curve. Multiple repetitions of the measurements were used to assess the associated error. Only results in which ohmic contacts and p-type activity were confirmed unambiguously are reported here.

2.4. SIMS

SIMS analysis was performed on sample types A and C (annealed at all four temperatures) and of the as-implanted sample for the dose of $1 \times 10^{15} \text{ cm}^{-2}$ (dose A). Samples nominally 1 cm^2 were analyzed with a Cameca IMS-3f ion microprobe using a positive oxygen beam and monitoring various positive secondary ions of interest. Concentration versus depth plots were extracted with depth scales obtained by measuring the SIMS craters with a Tencor P-10 surface profilometer. The indium profiles have been quantified by

using a relative sensitivity factor obtained from the as-implanted sample for which minimal dose loss is anticipated. Under these analytical conditions the indium detection limit was near $10^{16} \text{ atoms cm}^{-3}$. The quantification accuracy depends predominately on the depth scale calibration and is estimated to be approximately $\pm 10\%$.

3. Results and discussion

3.1. Electron microscopy analysis

HAADF STEM analysis of the as-implanted samples corresponding to doses A and C (not shown) indicates that the silicon matrix has been fully amorphized to a depth of ≈ 50 nm, as expected based on the implantation energy. Figure 1 presents low magnification HAADF STEM images from the dose A and C samples annealed at 650, 750 and 950 $^\circ\text{C}$; HAADF STEM images of samples annealed at 1050 $^\circ\text{C}$ indicate the same trend as samples annealed at 950 $^\circ\text{C}$ for both doses and are therefore not shown. There are three key points to note from figure 1, which will be discussed in turn:

- Indium precipitates are observed on the surface and in the regrown matrix for all of the dose A (highest dose) samples regardless of annealing temperature.
- The crystalline silicon matrix has not fully regrown to the surface in the A600 (highest dose, lowest anneal temperature); a nominally amorphous layer ≈ 10 nm thick is immediately below the surface and the amorphous–crystalline interface (henceforth referred to as the a–c interface) is visible.
- Indium precipitates are observed on the surface and in the regrown matrix for the C600 and C750 (mid dose, lower anneal temperatures) samples but not the C950 and C1050 (mid dose, higher anneal temperatures) samples.

In addition, we will also discuss the following results, based on detailed analysis of the electron microscopy data:

- The indium precipitates on the surface and in the matrix have a tetragonal crystal structure and an aspect ratio of ≈ 1.1 .
- While the indium precipitates are obvious in the HAADF STEM images (and verified by EEL SI), they are *not* readily visible in the bright field (BF) CTEM images.

When precipitates are observed in the silicon matrix, they exist within ≈ 50 nm of the surface, i.e. within the depth expected based on the implant energy, as highlighted by the thick dashed line on the left-hand side of each image included in figure 1, which indicates 50 nm from the surface. For the higher dose (dose A), precipitates showing increased intensity compared to the regrown silicon matrix are observed both on the surface and in the regrown crystalline matrix at all annealing temperatures. STEM EEL SI was used to verify that the precipitates have a strong indium $\text{M}_{4,5}$ edge signal (henceforth referred to as the indium signal). Figure 2 presents a HAADF STEM image and corresponding STEM EEL SI data corresponding to a precipitate embedded in the regrown silicon matrix from sample A750 and representing a typical embedded precipitate. The HAADF STEM overview image

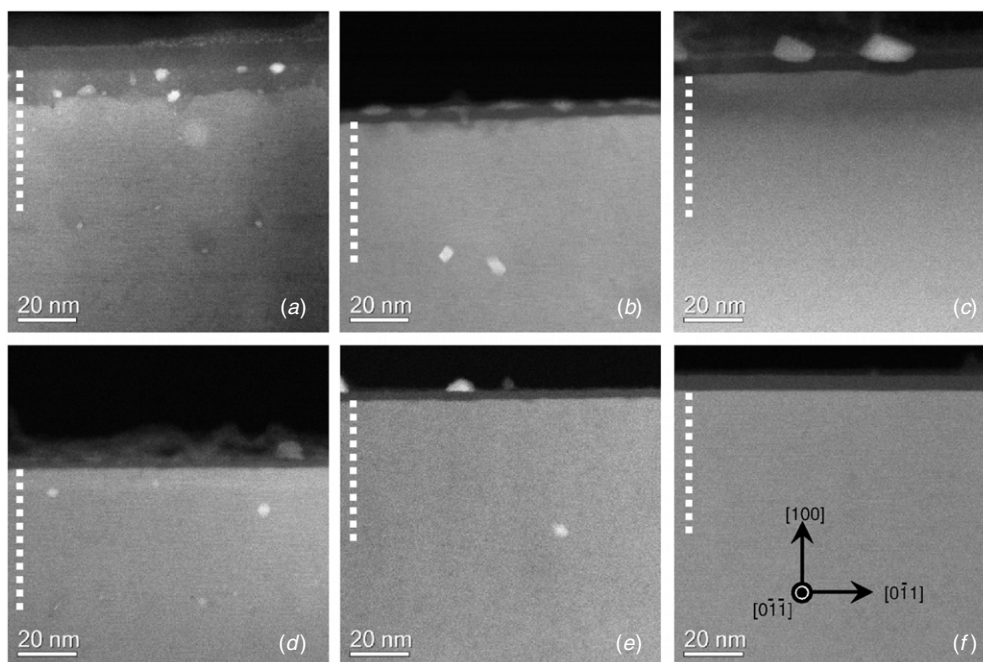


Figure 1. Low magnification HAADF STEM images showing an overview of the dose A (a)–(c) and C (d)–(f) samples annealed at 600 °C (a), (d), 750 °C (b), (e) and 950 °C (c), (f). In all images the sample surface is towards the top of the image and the thick dashed line on the left-hand side of the image indicates the extent of the implant depth (≈ 50 nm); crystallographic directions are shown on (f).

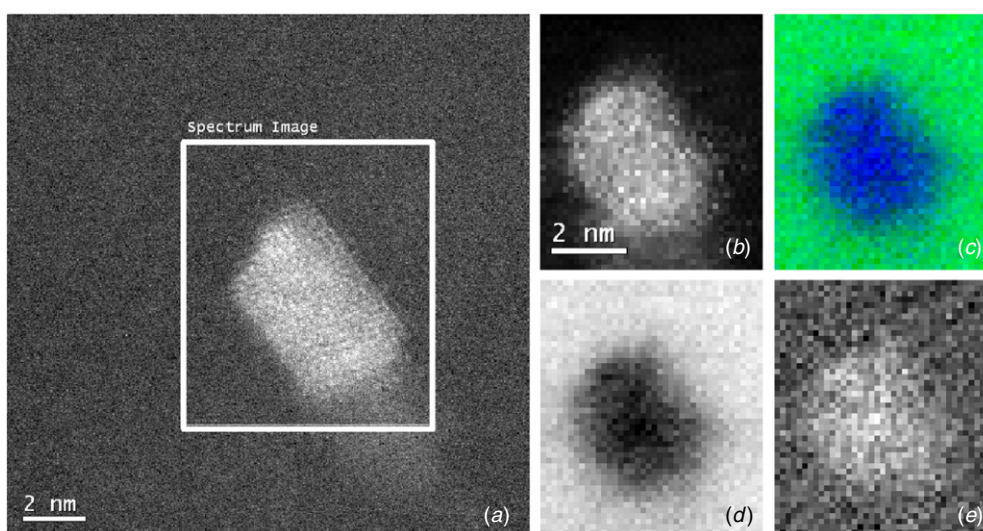


Figure 2. (Colour online) HAADF STEM and EEL SI data corresponding to a typical embedded precipitate (this example is from sample A750). (a) Overview HAADF STEM image showing a box around the region of interest where the spectrum image data was collected for elemental mapping shown in (b) to (e). (b) HAADF STEM image acquired from the region of interest simultaneously with the EEL data. (c) Spectrum image of the silicon (green) and indium (blue) signals overlaid. (d) Spectrum image of the silicon signal. (e) Spectrum image of the indium signal.

is shown in figure 2(a), with a box indicating the region where the spectrum image was acquired. Figure 2(b) shows the HAADF STEM image of the region of interest, acquired simultaneously with the EEL data, while (d) and (e) show maps of the silicon $L_{2,3}$ edge signal (henceforth referred to as the silicon signal) and indium signal, respectively. From figures 2(d) and (e), it is noted that the silicon signal decreases as the indium signal increases, highlighted in figure 2(c) where the silicon and indium signals have been overlaid. There is no

indication of any other elemental edges (e.g. oxygen K edge, henceforth referred to as the oxygen signal) or of any silicon–indium intermetallic formation, consistent with the silicon–indium phase diagram [14].

For the highest dose (dose A) and lowest annealing temperatures, we observe evidence of a ‘snow plough’ effect, whereby the indium segregates preferentially to the a–c interface and is ‘pushed’ towards the surface as the silicon matrix is regrown during annealing, slowing the regrowth. This

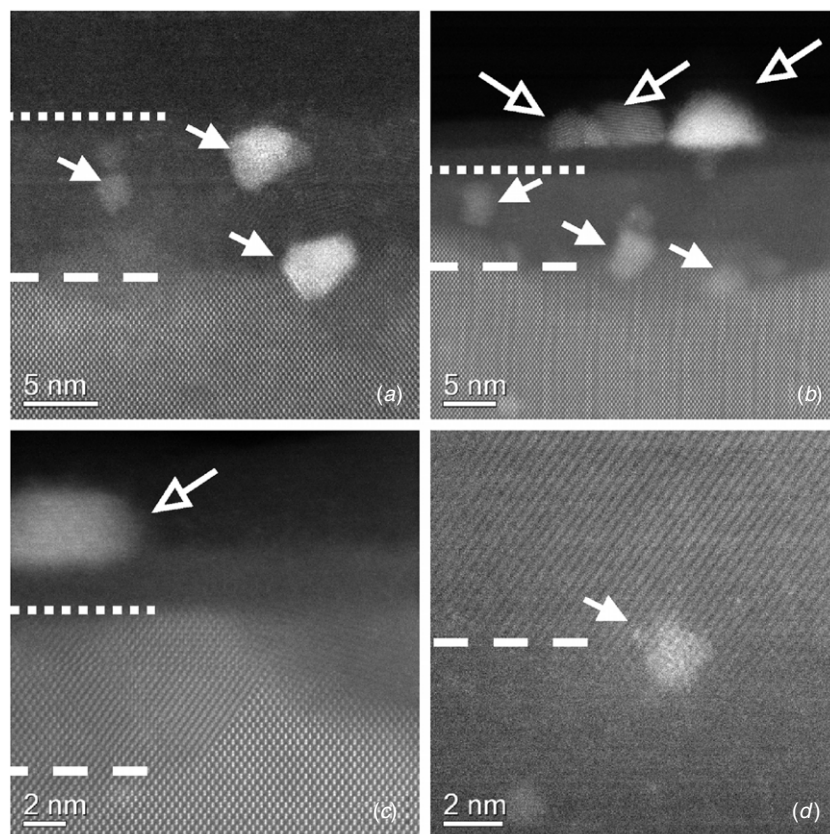


Figure 3. HAADF STEM images of sample A600 showing the ‘snow plough’ effect. In all images, if the top surface of the sample is in the image field-of-view it is indicated by a thick dotted line, the amorphous–crystalline interface is indicated by a thick dashed line, indium precipitates in the nominally amorphous layer near the surface and at the a–c interface are indicated by filled arrows and indium precipitates on the surface are indicated by unfilled arrows. (a) Indium precipitates near the surface in both the nominally amorphous layer and at the a–c interface. (b) Indium precipitates on the surface (on top of a thin native oxide), in the nominally amorphous layer, and at the a–c interface. (c) Indium precipitate on the surface near an area where the nominally amorphous layer shows polycrystalline fringes near the same orientation as the regrown silicon matrix. (d) The silicon matrix has been tilted to $\approx 4^\circ$ off of the $[0\bar{1}1]$ direction and crystalline fringes can be observed in the nominally amorphous layer near the surface, indicating it has crystalline structure; an indium precipitate is observed at the a–c interface.

has been observed previously for a variety of implant species including arsenic, fluorine, indium and phosphorous [15–20]. This is particularly evident in the A600 sample (highest dose, lowest annealing temperature), where an ≈ 10 nm thick nominally amorphous layer exists near the surface. In some cases, the amorphous layer shows signs of polycrystallinity. Figure 3 presents a series of images from the A600 sample in which the top surface of the sample (below the screen oxide) is highlighted with a thick dotted line and the a–c interface is highlighted with a thick dashed line. In figure 3(a), indium precipitates having a rectangular shape with side lengths ranging from 2–5 nm were observed at the a–c interface and in the nominally amorphous layer, while in figure 3(b), indium precipitates are observed on the surface as well. An example of a polycrystalline region within the nominally amorphous layer can be observed in figure 3(c), where a region of epitaxially regrown silicon having lower contrast than the matrix can be seen on the left-hand side of the image. This reduced contrast could be the result of changes to the electron channeling conditions due to, for example, imperfect silicon regrowth throughout the entire sample thickness (i.e. polycrystalline silicon in the direction of the electron beam). Further evidence

of polycrystallinity is demonstrated in figure 3(d), where the silicon matrix has been tilted away from the $[0\bar{1}1]$ zone axis condition. In this case, crystalline fringes *are not* visible in the silicon matrix below the a–c interface, yet fringes *are* visible in the nominally amorphous layer above the a–c interface (i.e., lattice fringes are observed above the thick dashed line); note that there is an indium precipitate at the a–c interface, on the right-hand side of the figure 3(d).

Figure 4 presents EEL SI data corresponding to the precipitates at the a–c interface and in the nominally amorphous layer above a–c interface, shown in figure 3(a). Figure 4(a) presents the overview HAADF STEM image with the region of the spectrum image data collection indicated, while (b), (d), (e) and (f) present the simultaneously acquired HAADF STEM image, and silicon, indium and oxygen spectrum image maps (respectively). Figure 4(c) shows the three spectrum image maps overlaid. This data confirms the presence of indium in the region of the precipitates (higher intensity in the HAADF STEM images). Near the top of the maps in (c) and (f), there is a significant oxygen signal originating from the native oxide on the surface of the sample. These maps also show a random low intensity oxygen signal

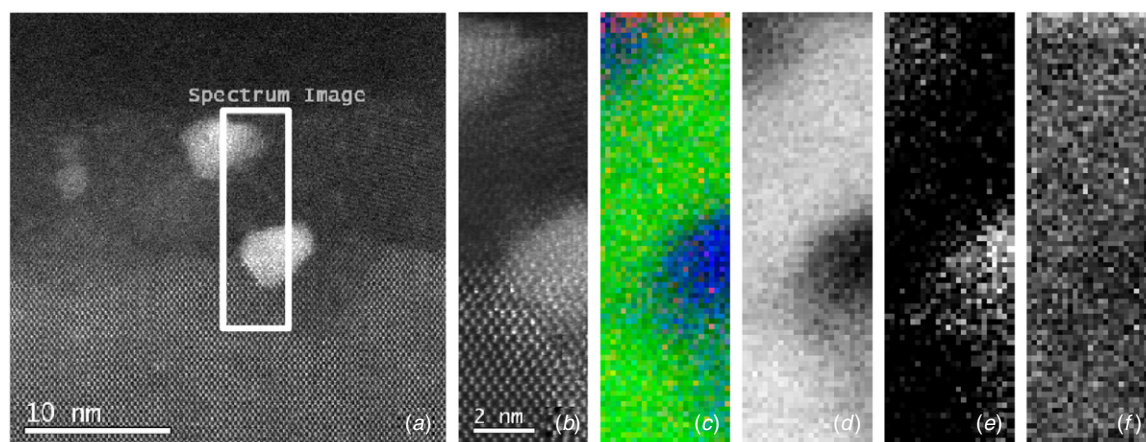


Figure 4. (Colour online) HAADF STEM and EEL SI data corresponding to the precipitates shown in figure 3(a). (a) Overview HAADF STEM image showing a box around the region of interest where the spectrum image data was collected. (b) HAADF STEM image acquired from the region of interest simultaneously with the EEL data. (c) Spectrum image of the silicon (green), indium (blue) and O (red) signals overlaid. (d) Spectrum image of the silicon signal. (e) Spectrum image of the indium signal. (f) Spectrum image of the O signal.

throughout the spectrum image field-of-view. This is expected to be a result of the overlap of the indium $M_{4,5}$ and oxygen K edges (at energy losses of 443 and 532 eV, respectively). That is, when performing the background subtraction for the oxygen K edge, there will be some contribution due to the overlapping indium $M_{4,5}$ signal and this may lead to an overestimation of the oxygen signal or apparent presence of oxygen in areas containing indium. The distribution and magnitude of the oxygen signal present in the spectrum image maps does not indicate a concentration of oxygen near the region of the precipitates at the a–c interface, in the nominally amorphous layer or on the surface (data not shown). This is in agreement with the data from the precipitates in the regrown silicon matrix (e.g., figure 2) and with the silicon–indium phase diagram [14].

As shown in figure 1, surface precipitates were observed in the dose A samples for all annealing conditions, but only in the lowest temperature annealing conditions for the dose C samples (C600 and C750). It is not clear why the precipitates do not appear in the C950 and C1050 samples, but we can speculate that indium is evaporated from the surface at these higher temperatures. In the case of the dose A samples, the higher dose may result in enhanced indium out-diffusion, such that the indium cannot evaporate entirely in the relatively short (2 min) annealing time.

All surface precipitates observed were on top of the surface oxide layer. Surface precipitates showing crystalline fringes, as observed in figure 5(a), were frequently observed in all dose/anneal conditions showing surface precipitates when the silicon matrix was aligned on the $[0\bar{1}\bar{1}]$ zone axis. Only one example of surface precipitates aligned to a zone axis orientation was observed, shown in figure 5(c). This suggests that the surface precipitates tend to have a crystalline structure but are not necessarily aligned to the regrown silicon matrix. Because only one precipitate aligned to a zone axis condition was observed, we cannot comment on the specific crystalline structure of the surface precipitates with confidence. We can though assert that EEL SI data indicates that the precipitates do not contain silicon.

Embedded precipitates in the regrown silicon matrix having a rectangular shape were observed for both doses A and C when annealed at 600 and 750 °C. By tilting the regrown silicon matrix away from the $[0\bar{1}\bar{1}]$ zone axis, the structure of the precipitates was deduced. Figure 5(b) presents a typical example of an embedded precipitate imaged with the silicon oriented on the $[0\bar{1}\bar{1}]$ zone axis, whereas figure 5(d) presents a typical example of the case when the silicon has been tilted away from the zone axis conditions. The aspect ratio of the precipitates was measured as 1.2 ± 0.1 (46 measured) with precipitates tending to have sides parallel to silicon $\{111\}$ planes. While the aspect ratio remains constant, the side lengths range from 2 to 5 nm depending on the sample, with the dose A samples having smaller precipitates than the dose C samples for the same annealing conditions, as shown in figure 6.

As discussed previously and as demonstrated in figure 2, EEL SI data taken from embedded precipitates indicates that they are not an indium–silicon mix, but rather pure indium. The structure of the precipitates was determined by comparing the HAADF STEM images (similar to that shown in figure 5(d)) to simulated images of bulk cubic (the lattice of bulk silicon) and tetragonal (the lattice of bulk indium) crystals. Three lattice spacing distances and one angle between crystallographic planes were measured from HAADF STEM images of 11 unique precipitates. Comparison of the data (including ratios of spacings/angles) demonstrated that the experimental data was inconsistent with all projections except the tetragonal $\langle 111 \rangle$ projection. Using the mean lattice spacing data from 11 precipitate images the lattice vectors of the precipitates were determined as $a = 0.31 \pm 0.01$ nm and $c = 0.45 \pm 0.01$ nm, compared to $a = 0.459$ nm and $c = 0.494$ nm for bulk indium; models of the bulk indium lattice and proposed precipitate lattice are shown in figure 7.

One interesting aspect of the precipitate analysis is the comparison of the defect and precipitate structures as observed in HAADF STEM mode versus BF CTEM mode. Prior to HAADF STEM characterization, all TEM samples were analyzed using BF CTEM. When comparing the same areas in

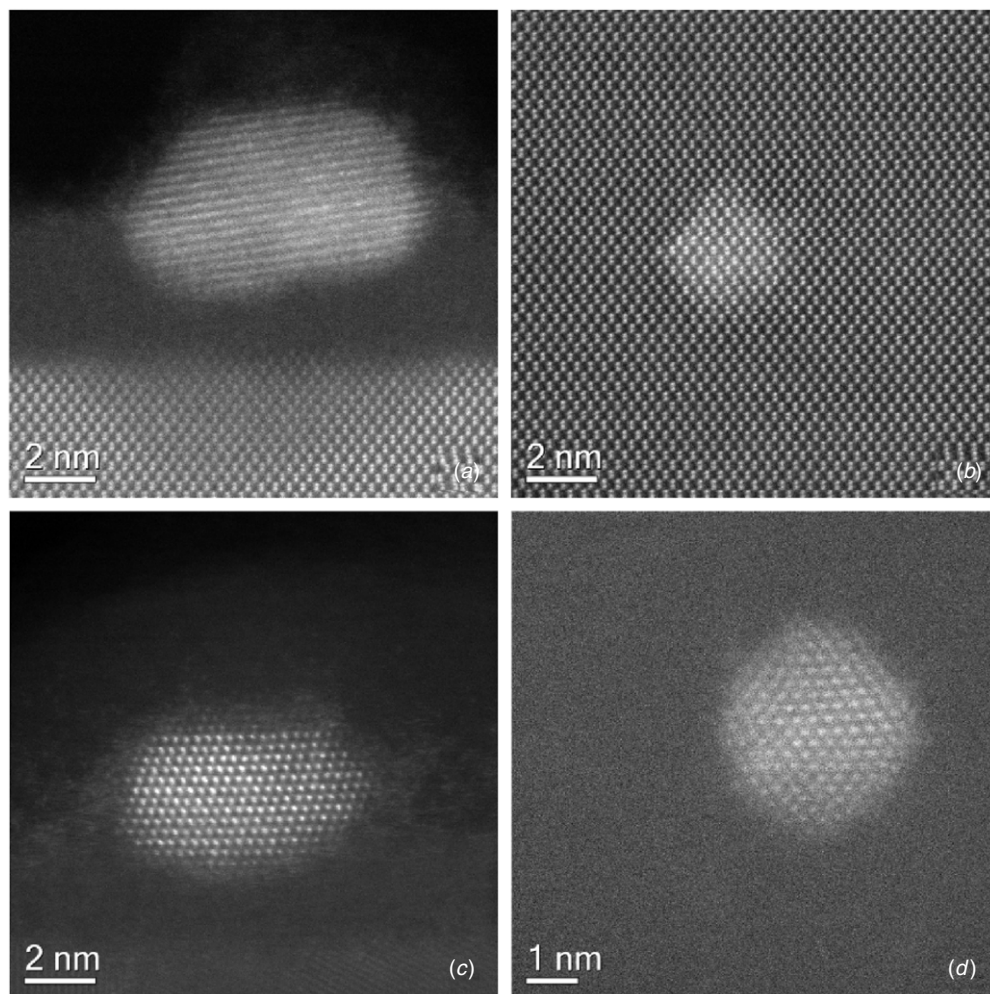


Figure 5. HAADF STEM images showing typical indium precipitates. (a) Lattice fringes in a precipitate on the surface of the fully regrown silicon matrix (silicon on $[0\bar{1}1]$ zone axis). (b) Precipitate embedded in the regrown silicon matrix (silicon on $[0\bar{1}1]$ zone axis). (c) Atomic structure of a precipitate on the surface of the fully regrown silicon matrix (silicon on $[0\bar{1}1]$ zone axis). (d) Atomic structure of a precipitate embedded in the silicon matrix (silicon tilted 4° away from $[0\bar{1}1]$ zone axis).

BF CTEM and HAADF STEM, we noticed that the visibility of the embedded precipitates varied significantly between the two techniques. Figure 8 presents a typical area of the A600 sample as imaged by BF CTEM and HAADF STEM (images have been rotated and scaled so that the same size region is shown for both techniques). The a–c interface and nominally amorphous silicon layer near the surface of the sample (where the silicon matrix has not fully regrown) can be discerned using both techniques (highlighted by the solid red lines and large circle). However, the embedded indium precipitates, which can be observed as high intensity regions in the HAADF STEM image (highlighted by the small dotted green circles), are not clearly visible in the BF CTEM image.

This comparison of the HAADF STEM and BF CTEM suggests that BF CTEM images may not necessarily be useful for assessing the distribution of indium precipitates in the regrown silicon matrix, and may warrant reconsideration of the conditions used in previous BF CTEM studies into heavy dopants in silicon where dopant concentrations were expected to be near or above the solid solubility but no evidence of precipitates was found from BF CTEM [1]. It is also worth

noting that the extended $\{311\}$ defects at the end-of-range (highlighted in medium-sized dashed yellow circles) appear with much higher contrast in the BF CTEM image than the HAADF STEM image, highlighting the value of BF CTEM for investigating the number/length of such defects. In this case HAADF STEM offers the potential for high resolution observation and characterization [21].

3.2. Resistivity and Hall measurements

The electrical measurement of the prepared samples are summarized in figure 9. Reproducible measurements were obtained from the majority of samples, although for all samples annealed at 600°C no significant electrical activity was observed (e.g. contacts were non-ohmic). This is likely a result of the large volume of defects remaining following the annealing step, evidenced by the electron microscopy results reported above. Also, despite repeated attempts at sample preparation, no significant electrical activity was observed from the sample A1050. We note that for the relatively low concentrations of activated dopant in the present case, a

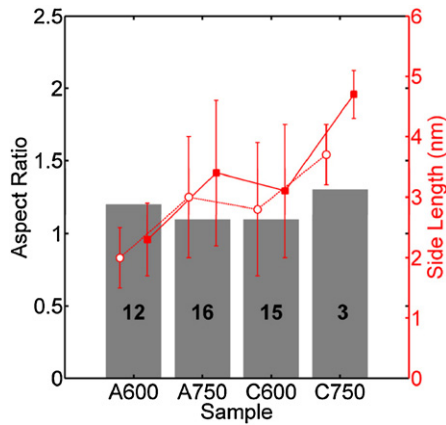


Figure 6. (Colour online) Aspect ratio (filled bars, left-hand y-axis) and side lengths (filled squares and open circles, right-hand y-axis) for precipitates in the A650, A750, C650 and C750 samples. Numbers shown on the bars indicate the number of precipitates measured in each case and error bars on side lengths represent the standard deviation of the measurements. Filled squares and open circles used for plotting side lengths indicate the long and short side lengths, respectively.

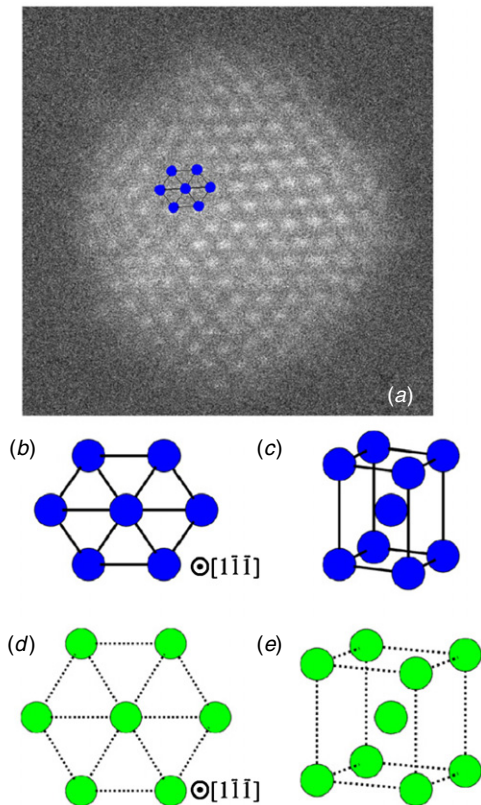


Figure 7. (Colour online) (a) Enlarged region of the HAADF STEM image shown in figure 5(d) (image size is 5 nm^2), with a unit cell from the proposed model overlaid. The proposed indium precipitate model unit cell as viewed in (b) the $[1\bar{1}\bar{1}]$ direction and (c) 3D perspective. The unit cell of bulk indium as viewed in (d) the $[1\bar{1}\bar{1}]$ direction and (e) 3D perspective is shown for reference.

depletion region will extend into the indium doped layer from the n-doped substrate. This depletion may be as much as tens of nanometers for an active concentration of a few 10^{17} cm^{-3} . Correction for this effect is non-trivial and is not attempted

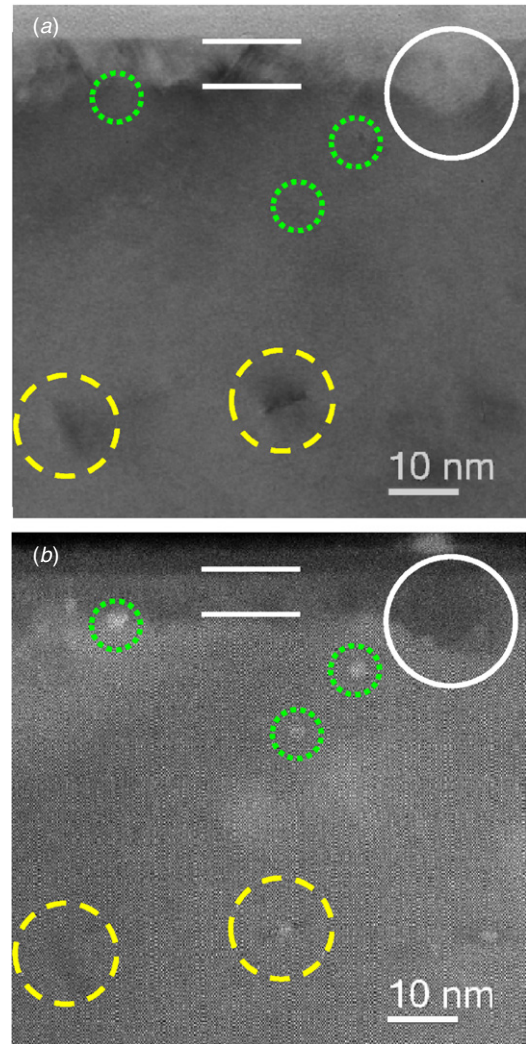


Figure 8. (Colour online) Comparison of (a) BF CTEM and (b) HAADF STEM images of the same region from the A600 sample. The solid white lines parallel to the surface indicate the $\approx 10 \text{ nm}$ thick nominally amorphous layer, while the largest circle, outlined with a solid white line, indicates a polycrystalline region within this layer. The smallest circles, outlined with dotted green lines, highlight the position of the indium precipitates, while the medium-sized circles, outlined with dashed yellow lines, indicate extended $\{311\}$ defects near the end-of-range.

here. It will have most impact on the results for the shallowest junctions, which are obtained after annealing at 750°C . In this case the sheet carrier concentration may be underestimated by as much as 100%. The use of an n-type substrate provides a depletion region between the doped layer and the substrate. We estimate that the shunt resistance in our case is at least one order of magnitude greater than the sheet resistance of the doped layer. Consistent p-type activity (as measured) would suggest also that the overwhelming majority of current flow is via activated holes.

The results reveal similar electrical characteristics despite the wide range in implanted dose and annealing temperature. The free hole sheet concentration ranges from $1\text{--}3.5 \times 10^{12} \text{ cm}^{-2}$, except for B1050 in which a concentration of $\approx 6 \times 10^{12} \text{ cm}^{-2}$ is observed. This behavior is indicative of a limit in the amount of implanted indium which may

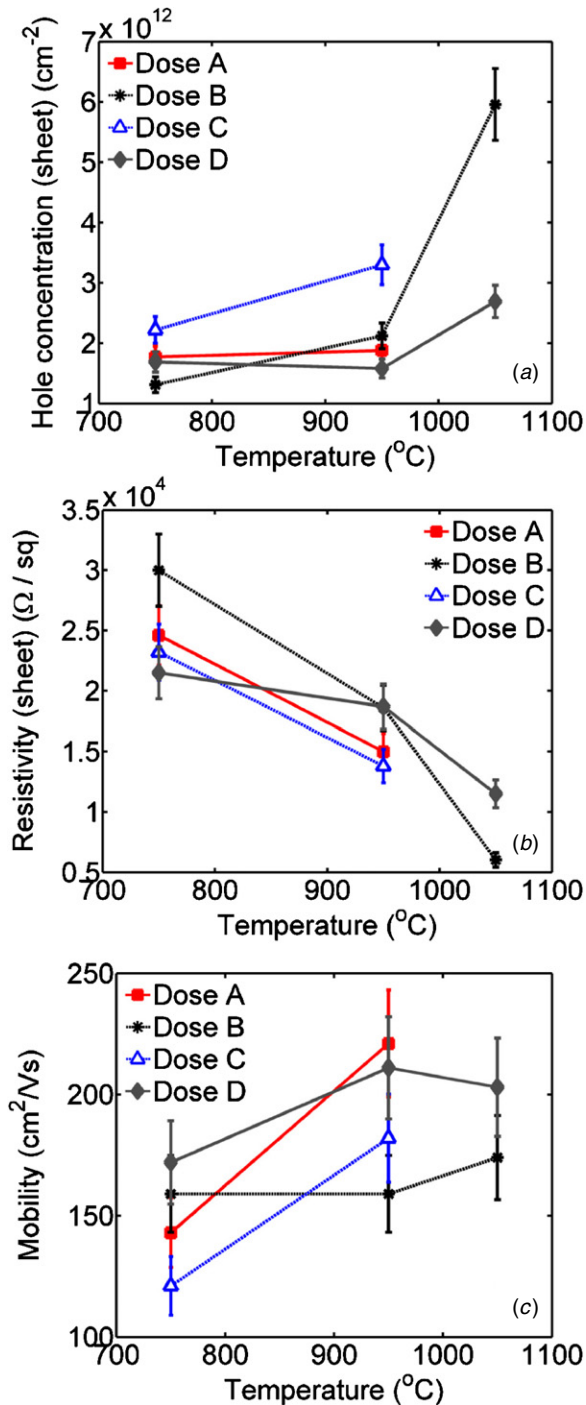


Figure 9. (a) Hole concentration (sheet) (cm^{-2}), (b) resistivity (sheet) (Ωsq^{-1}) and (c) mobility ($\text{cm}^2 \text{V}^{-1} \text{s}^{-1}$) for doses A, B, C and D, plotted as a function of increasing temperature.

be activated electrically and it is tempting to deduce a solid solubility for indium in silicon from these measurements which is of the order of $1\text{--}3 \times 10^{18} \text{ cm}^{-3}$ (assuming the activated indium is concentrated in the first 100 nm from the sample surface as is indicated for samples annealed at 750 and 950 °C). The excess indium either clusters into electrically inactive inclusions, or is lost through the sample surface as indicated by the electron microscopy. Indeed, the surface evaporation accounts for a significant loss mechanism in terms of inactive

indium and will be discussed further below. The sheet resistivity decreases for all samples with increasing annealing temperature. This is consistent with expected removal of implantation induced defects and the break-up of large indium inclusions, both of which are likely to act as carrier scattering centers. However, we cannot claim with any certainty that a corresponding increase in mobility is observed, due mainly to the error associated with the measurement. We would also expect an increase in mobility as a result of reduced ionized impurity scattering, an effect highlighted by the SIMS results and discussed below. As annealing temperature increases, the indium experiences increasing diffusion and thus the peak concentration reduces, decreasing the expected ionized impurity scattering. Values for hole mobility are found to range between $120\text{--}220 \text{ cm}^2 \text{V}^{-1} \text{s}^{-1}$, which compares well with previous reports [22], although we again note that trends in the mobility are not distinguishable in the current data set. Despite the marginal improvement in electrical characteristics (e.g. approximately halving the sheet resistivity, as shown in figure 9(b)) with increased post-implantation annealing, we will discuss in the following section the need to limit the annealing temperature to below 950 °C (and more likely close to 750 °C) for these implantation conditions if the as-implanted indium profile is to be maintained.

3.3. SIMS

The indium concentration profiles for doses A and C (all annealing conditions) are plotted in figure 10. In each panel we include the profile of the as-implanted sample (dose A) used to calibrate all samples to absolute concentration. The evolution of the profiles with increasing annealing temperature is consistent with previous work [1]. For temperatures 600, 750 and 950 °C indium is accumulated to a depth consistent with the end-of-range of the initial implant ($\approx 60 \text{ nm}$ from the surface). For amorphizing implantations such as those used here, large numbers of defects are expected to persist at the end-of-range even after annealing, and it is these defects which efficiently trap excess indium. There also appears a significant segregation occurring at the surface of the sample, and thus a two-peaked appearance of the profile emerges. For an annealing temperature of 750 °C (a temperature for which significant electrical activation occurs) there is a relatively small amount of diffusion of indium compared with the as-implanted profile, with the junction depth (here defined as the point at which concentration falls to 10^{16} cm^{-3}) increasing from 130 to 190 nm. For both dose A and C, this junction depth increases significantly for an annealing temperature of 950 °C to $>300 \text{ nm}$ while for 1050 °C the junction depth can only be estimated from the present SIMS data to be $>600 \text{ nm}$. Strikingly, for this highest anneal temperature the peak concentration of indium has dropped to $<10^{17} \text{ cm}^{-3}$. These trends are consistent with significant enhanced diffusion usually associated with the break-up of silicon interstitial clusters, which are known to be present in the implanted material.

It is interesting and instructive to consider the retained dose as compared to the implanted dose for the current

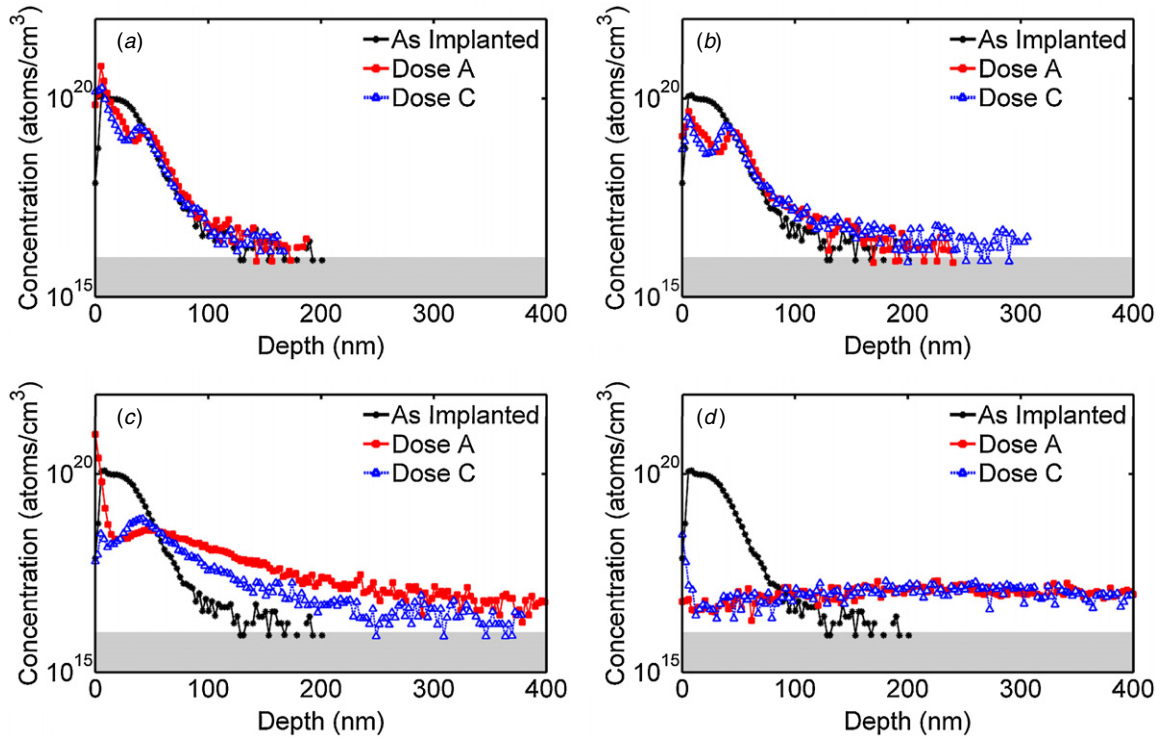


Figure 10 (Colour online) SIMS results for indium concentration as a function of depth comparing doses A and C for (a) 600 °C, (b) 750 °C, (c) 950 °C and (d) 1050 °C. The gray shaded region indicates the minimum sensitivity level of $\approx 10^{16}$ atoms cm^{-3} and the SIMS data from the as-implanted sample is shown for reference.

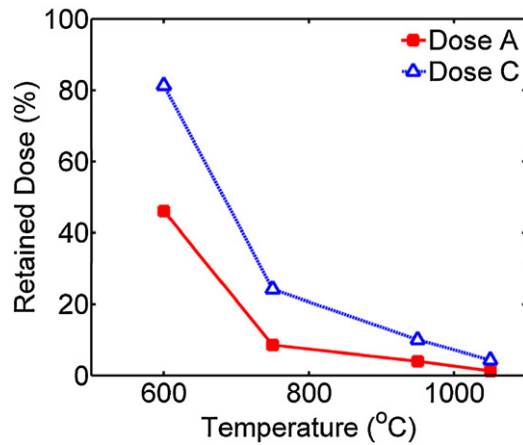


Figure 11. SIMS percentage retained dose for doses A and C.

samples. The retained dose for indium in silicon has been noted previously to be as low as 30% for an implantation at a dose and energy of $7 \times 10^{12} \text{ cm}^{-2}$ and 150 keV, respectively, and subsequently annealed at 1000 °C [1]. The retained dose for the current samples derived from the SIMS measurements is plotted in figure 11. We note that the values for A1050 and C1050 are underestimated due to the incomplete measurement of the entire indium profile in these cases. Significant dose loss is observed even at an annealing temperature of 600 °C, before any electrical activation is measured. For higher annealing temperatures the retained dose reduces dramatically until it is $< 10\%$ for all samples annealed at or above 750 °C, with the exception of C750 for which it is $\approx 25\%$. This result suggests that dose loss through the surface of the sample is significant if

Table 1. Percentage of activated carriers over retained dose for samples A750, A950, C750 and C950.

Anneal temperature (°C)	Dose A	Dose C
750	2%	3%
950	5%	11%

not dominant in accounting for the lack of activated indium in these samples. For example, for sample C750, we may consider the total sheet concentration of indium within the sample to be $\approx 7.5 \times 10^{13} \text{ cm}^{-2}$ (i.e. 25% of the implant dose, $3 \times 10^{14} \text{ cm}^{-2}$, is retained, shown in figure 11); whereas the free hole concentration is $2.4 \times 10^{12} \text{ cm}^{-2}$ (shown in figure 9(a)). If we assume that due to the position of the indium level in the bandgap ($E_v + 157 \text{ meV}$) we have an activation fraction of $\approx 10\%$ [23], we can reasonably assume that 68% of the indium present in the sample is inactive and likely in the form of precipitates, whereas 75% of the initial implanted dose has been lost through the surface during the activation anneal. Table 1 presents the percentage of activated carriers over retained dose for samples A750, A950, C750 and C950.

In order to compare the SIMS and HAADF STEM results in a more quantitative manner, the concentration of indium in the form of precipitates was estimated using low magnification HAADF STEM images (magnifications similar to those used in figure 1). Several approximations and/or assumptions were made in this process, including:

- Indium precipitates embedded below the specimen surface were treated as cubes, the number of which were divided into volume bins.

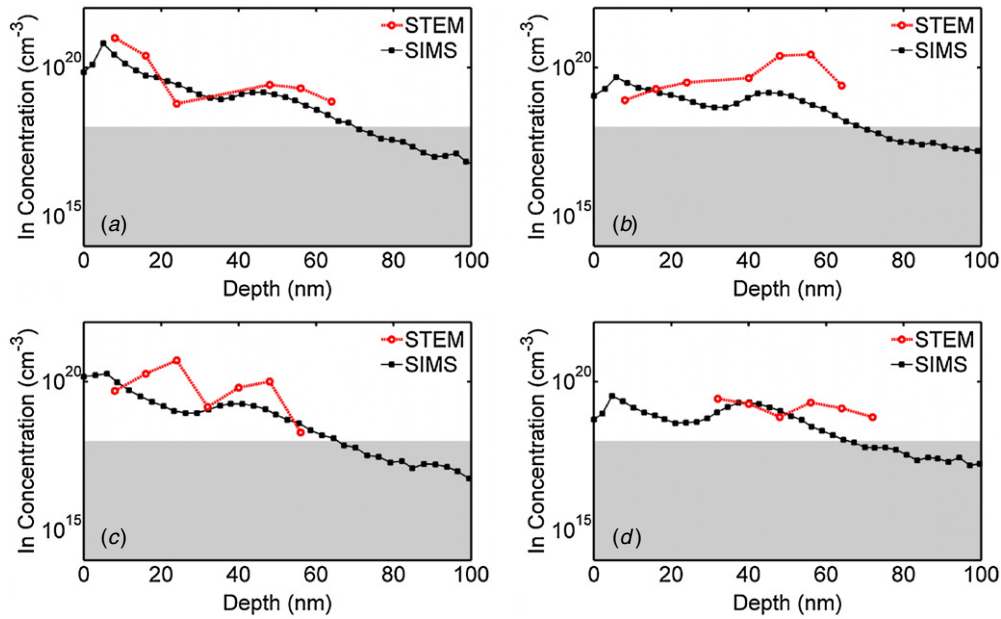


Figure 12. Comparison of indium concentration (atoms cm^{-3}) as a function of depth measured from low magnification HAADF STEM images and SIMS data for (a) A600, (b) A750, (c) C600 and (d) C750 samples. The shaded region indicates indium concentrations below $10^{18} \text{ atoms cm}^{-3}$.

- Atomic volume of indium in precipitate form was assumed to be the same as the atomic volume of bulk silicon ($\approx 5 \times 10^{22} \text{ atoms cm}^{-3}$).
- The specimen thickness $t = 50 \text{ nm}$ measured using the mean-free path of total inelastic scattering [13] in one area of the image field-of-view was assumed to be constant over the entire image field-of-view.

For each precipitate, side lengths and centroid positions were measured and the volume calculated. The field-of-view was divided into bins having a width equal to 8 nm in the [100] direction (i.e. perpendicular to the surface), and the precipitate volume in each bin was calculated. Fractional volumes were allowed, for example if a precipitate had a centroid position of 8 nm from the surface, then half of the volume would be contained in the bin from 0 to 8 nm and half in the bin from 8 to 16 nm. The total precipitate volume in each bin was converted into indium concentration in cm^{-3} by multiplying by the atomic volume of silicon and dividing by the volume of the bin ($V_{\text{bin}} = 8 \text{ nm} \times t \times w$ where $t \approx 50 \text{ nm}$ is the specimen thickness and w is the image width, which varied depending on the image magnification). The number (N) of precipitates measured for each specimen depended on the concentration (29 measured for A600, 18 measured for A750, 30 measured for C600 and five measured for C750) and only the 600 and 750 °C anneal temperature samples were compared because only these samples had embedded precipitates, as observed in the HAADF STEM images.

Figure 12 presents a plot of the indium concentration as measured by SIMS and from the HAADF STEM images. In some cases the concentration measured by HAADF STEM appears to be greater than that measured by SIMS, which is not physical, rather this reflects the large fractional error associated with estimated the concentration of indium in precipitate form when only a few precipitates are present (and thus measured)

within the sample. For instance, for A600 (29 precipitates measured) the agreement between the HAADF STEM and SIMS is rather good, whereas for C750 (five precipitates measured) the absolute agreement is less satisfactory. In any case, we stress that these plots are an attempt for semi-quantitative comparison of the SIMS and HAADF STEM data only and that only the indium in precipitates is considered in the HAADF STEM analysis.

The first point of interest is that in all cases the precipitates observed in the HAADF STEM have a maximum depth of $\approx 60 \text{ nm}$, consistent with the implanted ion end-of-range depth. Comparing with the SIMS data, we observe that at this depth, the indium concentration is no greater than $\approx 10^{18} \text{ cm}^{-3}$, in agreement with previously published values for the solid solubility of indium in silicon [1] and our estimate of solid solubility from electrical measurement. Indeed, we offer these results as the first direct observation of indium clustering that confirm the solid solubility limit in a direct fashion. It is also of interest to note that in the case of samples A600, A750 and C600 (figure 12(a)–(c)), the HAADF STEM data shows precipitates distributed from the surface to the end-of-range depth, while in the case of the C750 sample (figure 12(d)), precipitates are not present from the surface to a depth of $\approx 30 \text{ nm}$, and then they appear for depths between 30 nm to the end-of-range. This suggests that the indium concentration within 30 nm from the surface, as measured by SIMS, may be sitting substitutionally on silicon lattice sites, and therefore electrically active.

4. Conclusions

We have investigated a series of indium doped silicon samples having indium concentrations expected to be well above the assumed solid solubility of indium in silicon

and annealed at temperatures between 600 and 1050 °C. We have compared electron microscopy, electrical (Hall) and SIMS data to develop a broad understanding of how the dopant behaves at these concentrations and annealing conditions. Our results provide evidence for nano-scale indium precipitates in the silicon matrix and on the surface after annealing. We observe these precipitates have a tetragonal crystal structure and rectangular shape with an aspect ratio of 1.2 ± 0.1 and side lengths ranging from 2 to 5 nm. Our results demonstrate that careful consideration of CTEM images is required in order to determine the presence of indium precipitates in the silicon matrix. While Hall data demonstrates improved electrical characteristics with increasing annealing temperature, SIMS analysis showed significant dose loss for annealing temperatures >750 °C; the retained dose is <25% for these temperatures. Our results indicate a solid solubility of $\approx 10^{18} \text{ cm}^{-3}$, consistent with previously published work [1].

Acknowledgments

KJD is grateful to the Ontario Ministry of Economic Development and Innovation for partial support of a Postdoctoral Fellowship. GAB is grateful to NSERC for a Discovery Accelerator Grant partially supporting of this work. The experimental microscopy work was carried out at the Canadian Centre for Electron Microscopy, a National Facility supported by NSERC and McMaster University. The SIMS analysis was performed at the Surface Science Western facility at the University of Western Ontario.

References

- [1] Solmi S, Parisini A, Bersani M, Giubertoni D, Soncini V, Carnevale G, Benvenuti A and Marmiroli A 2002 *J. Appl. Phys.* **92** 1361–6
- [2] Shahidi G G, Davari B, Bucelot T J, Ronsheim P A, Coane P J, Pollack S, Blair C R, Clark B and Hansen H H 1993 *IEEE Electron Device Lett.* **14** 409–11
- [3] Hu H, Jacobs J B, Su L T and Antoniadis D A 1995 *IEEE Trans. Electron Devices* **42** 669–77
- [4] Gennaro S, Collart E, Wang Y, Sealy B J and Gwilliam R M 2003 *Nucl. Instrum. Methods Phys. Res. B* **209** 136–9
- [5] Gennaro S, Sealy B J and Gwilliam R M 2005 *Electron. Lett.* **41** 1302–4
- [6] Scalese S, Grasso S, Italia M, Privitera V, Christensen J S and Svensson B G 2006 *J. Appl. Phys.* **99** 113516
- [7] Scalese S, Italia M, La Magna A, Mannino G, Privitera V, Bersani M, Giubertoni D, Barozzi M, Solmi S and Pichler P 2003 *J. Appl. Phys.* **93** 9773–82
- [8] Lulli G, Bianconi M, Parisini A and Napolitani E 2004 *J. Appl. Phys.* **95** 150–5
- [9] Stolk P A, Gossmann H J, Eaglesham D J, Jacobson D C, Rafferty C S, Gilmer G H, Jaraiz M, Poate J M, Luftman H S and Haynes T E 1997 *J. Appl. Phys.* **81** 6031–50
- [10] Noda T 2002 *J. Appl. Phys.* **91** 639–45
- [11] Pennycook S J and Jesson D E 1991 *Ultramicroscopy* **37** 14–38
- [12] Hartel P, Rose H and Dinges C 1996 *Ultramicroscopy* **63** 93–114
- [13] Egerton R F 1996 *Electron Energy-Loss Spectroscopy in the Electron Microscopy* 2nd edn (New York: Plenum)
- [14] Olesinski R W, Kanani N and Abbaschian G J 1985 *Bull. Alloy Phase Diagr.* **6** 128–30
- [15] Williams J S and Elliman R G 1982 *Appl. Phys. Lett.* **40** 266–8
- [16] Williams J S 1983 Solid phase recrystallisation processes in silicon *Surface Modification and Alloying by Laser, Ion and Electron Beams* ed J M Poate (New York: Plenum) p 142
- [17] Zechner C, Matveev D and Erlebach A 2004 *Mater. Sci. Eng. B* **114** 162–5
- [18] Ruffell S, Mitchell I V and Simpson P J 2005 *J. Appl. Phys.* **98** 083522
- [19] Suzuki K, Kataoka Y, Nagayama S, Magee C W, Buyuklimanli T H and Nagayama T 2007 *IEEE Trans. Electron Devices* **54** 262–71
- [20] Mirabella S, Impellizzeri G, Bruno E, Romano L, Grimaldi M G, Priolo F, Napolitani E and Carnera A 2005 *Appl. Phys. Lett.* **86** 121905
- [21] Dudeck K J, Marques L A, Knights A P, Gwilliam R M and Botton G A 2013 *Phys. Rev. Lett.* **110** 166102
- [22] Sze S M 2006 *Physics of Semiconductor Devices* 3rd edn (New York: Wiley-Interscience)
- [23] Green M A 1990 *J. Appl. Phys.* **67** 2944–54